Analytical solution of radiative transfer in the coupled atmosphere–ocean system with a rough surface

Zhonghai Jin, Thomas P. Charlock, Ken Rutledge, Knut Stamnes, and Yingjian Wang

Using the computationally efficient discrete-ordinate method, we present an analytical solution for radiative transfer in the coupled atmosphere–ocean system with a rough air–water interface. The theoretical formulations of the radiative transfer equation and solution are described. The effects of surface roughness on the radiation field in the atmosphere and ocean are studied and compared with satellite and surface measurements. The results show that ocean surface roughness has significant effects on the upwelling radiation in the atmosphere and the downwelling radiation in the ocean. As wind speed increases, the angular domain of sunglint broadens, the surface albedo decreases, and the transmission to the ocean increases. The downward radiance field in the upper ocean is highly anisotropic, but this anisotropy decreases rapidly as surface wind increases and as ocean depth increases. The effects of surface roughness on radiation also depend greatly on both wavelength and angle of incidence (i.e., solar elevation); these effects are significantly smaller throughout the spectrum at high Sun. The model-observation discrepancies may indicate that the Cox–Munk surface roughness model is not sufficient for high wind conditions.

OCIS codes: 010.1290, 010.4450, 030.5620.

1. Introduction

Cox and Munk[1] described the statistical characteristics of reflection by wind-blown ocean waves by modeling the sea surface as a collection of individual mirror facets. They presented the probability distribution for the slopes of surface facets as a wind-speed-dependent Gaussian function. Based on this Cox and Munk formulation, several researchers incorporated the ocean surface roughness in their radiative transfer models.[2–8] Most of these models used the ray-tracing method or the Monte Carlo technique to treat the surface roughness. The Monte Carlo approach consists of using probabilistic concepts and has the advantage for geometries other than the plane-parallel. Implementation of the statistical surface roughness by the Monte Carlo method is relatively straightforward. The discrete-ordinate technique, on the other hand, can be more computationally efficient and accurate, because it solves the radiative transfer equation analytically without the enormous statistical sample required to close a Monte Carlo solution and without the statistical fluctuation error. However, because of its analytical nature, implementation of the surface roughness in a discrete-ordinate radiative transfer code is more complicated; a rigorous solution involves an additional parameter that results in a different analytical solution from the flat surface case.

To extend applications of the Discrete-Ordinate Radiative Transfer (DISORT) code for systems including two media (atmosphere and ocean, atmosphere and ice, etc.), Jin and Stamnes[9] developed a coupled DISORT (CDISORT). The CDISORT code accounts for change in the refractive index at the boundary of the two media. For radiative transfer in such a coupled system, CDISORT treats the ocean or ice the same as atmospheric layers but with different optical properties, particularly, different refractive indices. However, the interface between two strata with different refractive indices was considered flat. This flat surface assumption limits the applications of CDISORT; the aforementioned wind-blown ocean surface is hardly flat. In addition to affecting reflec-

Z. Jin (z.jin@larc.nasa.gov) and K. Rutledge are with AS&M, Incorporated and NASA Langley Research Center, One Enterprise Parkway, Suite 300, Hampton, Virginia 23666. T. P. Charlock is with the Division of Atmospheric Sciences, NASA Langley Research Center, Mail Stop 420, Hampton, Virginia 23681-2199. K. Stamnes is with the Department of Physics and Engineering Physics, Stevens Institute of Technology, Hoboken, New Jersey 07030. Y. Wang is with the Anhui Institute of Optics and Fine Mechanics, Chinese Academy of Sciences, Hefei, Anhui 230031, China.

Received 4 January 2006; revised 6 March 2006; accepted 25 April 2006; posted 19 May 2006 (Doc. ID 67000).

0003-6935/06/287443-13$15.00/0

tion, the surface roughness itself significantly affects the directional character of the beam transmitted beneath the air–water interface. Gjerstad and coworkers[10] proposed an *ad hoc* method to consider the surface roughness in the discrete-ordinate method. They mimic the irradiances from a Monte Carlo model by adjusting the refractive index in CDISORT. This method has a number of limitations; for example, it calculates irradiances only in the ocean. Here we present a more consistent and widely applicable solution of the DISORT problem in the coupled atmosphere–ocean system with a rough surface.

2. Equation and Solution of Radiative Transfer

To incorporate ocean surface roughness into a radiative transfer equation and obtain an analytical solution through the discrete-ordinate method, we need to make the following assumptions:

- The rough surface can be resolved as a series of small planar facets, and the orientations (slopes) of these facets follow a certain statistical distribution, for example, the Gaussian distribution described by Cox and Munk.[1]
- The dimensions of the elemental facets and surface undulations are large compared with the wavelength of light, so geometrical optics can be applied to calculate the reflection and refraction at the surface.
- The optical depth of either the ocean or the atmosphere is independent of the surface roughness or horizontal position, because statistically there is no difference between any two points on the surface.

Under these assumptions, the time-averaged radiative effects at any two points on the surface are the same, and a patch of surface area at an instant in time in which every possible slope occurs can represent the surface as a whole. Therefore radiative transfer in a coupled system with a horizontally homogeneous atmosphere and ocean and with a rough ocean surface is still in the one-dimensional category, as long as the calculated radiation is considered to be time averaged (statistically averaged) for a point or to be relevant to a surface area larger than the patch aforementioned for an instant. We also treat the radiance and the reflection and refraction at the ocean surface as scalar. Therefore the model presented here should not be applied to problems where polarization is important.

Jin and Stamnes[9] (hereafter referred to as JS94) presented in detail the solution for coupled (i.e., air–sea) radiative transfer by the discrete-ordinate method for the flat ocean case. Here we will follow the same conventions defined in JS94 to describe the discrete-ordinate radiative transfer equation and solution for the rough surface case. Because the formulations have a lot in common between these two cases, we will omit most common derivations and emphasize the differences here.

For the flat surface case, the ocean was divided into a totally reflecting angular domain where upwelling photons cannot return directly to the atmosphere, and a refracting domain where upwelling photons can pass the interface directly to the atmosphere. However, once the surface roughness is introduced, there are no such distinct angular domains. Because of the possible ranges of orientations for the surface facets, photons in the atmosphere may pass the interface and direct to any angle downward, and vice versa for photons from the ocean to the atmosphere. This difference results in different radiative transfer solutions.

The radiative transfer equation to be solved for a plane-parallel medium with one dimension can be written as

$$\mu \frac{\mathrm{d}I(\tau,\ \mu,\ \phi)}{\mathrm{d}\tau} = I(\tau,\ \mu,\ \phi) - \frac{\omega(\tau)}{4\pi}\int_0^{2\pi} \mathrm{d}\phi' \times \int_{-1}^{1} p(\tau,\ \mu,\ \phi,\ \mu',\ \phi')I(\tau,\ \mu',\ \phi') \times \mathrm{d}\mu' + Q(\tau,\ \mu,\ \phi), \quad (1)$$

where $I(\tau, \mu, \phi)$ is the radiance at vertical optical depth τ (measured downward from the upper boundary) and in direction (μ, ϕ); μ is the cosine of the zenith angle (positive for upward directions); ϕ is the azimuth angle; ω is the single scattering albedo; and $p(\tau, \mu, \phi, \mu', \phi')$ and $Q(\tau, \mu, \phi)$ are the phase function and source term, respectively. We consider only the solar radiation (i.e., not terrestrially emitted thermal infrared or microwave). The solar-beam source, $Q(\tau, \mu, \phi)$, is different from the case of a flat ocean. In the flat surface case, part of the downwelling solar beam is reflected specularly back to the atmosphere, and the rest is refracted into the ocean at an angle, which depends on the refractive index; this results in two terms (downwelling and reflected) in the solar source function for the atmosphere [Eq. (3) in JS94] and one refractive index dependent term for the ocean [Eq. (4) in JS94]. However, for the case of a rough ocean, the solar beam is diffused to various directions when it hits the surface. Therefore there is no beam source term in the ocean and only one expression in the atmosphere for the rough ocean case, which is

$$Q(\tau,\ \mu,\ \phi) = \begin{cases} \omega(\tau)/4\pi F_0 p(\tau,\ \mu,\ \phi,\ -\mu_0,\ \phi_0)\exp(-\tau/\mu_0), & \tau \le \tau_a, \\ 0, & \tau > \tau_a, \end{cases} \quad (2)$$

where τ_a is the total optical depth of the atmosphere, μ_0 is the cosine of the solar zenith angle, ϕ_0 is the solar azimuth angle, and F_0 is the solar-beam intensity at the top of the atmosphere.

Expanding the radiance $I(\tau, \mu, \phi)$ into a Fourier cosine series of $2N$ and the phase function $p(\tau, \mu, \phi, \mu', \phi')$ into a series of $2N$ Legendre polynomials, the discrete-ordinate method converts Eq. (1) into a system of azimuthally independent, coupled differen-

tial equations for each of the Fourier components. Detailed derivations of these equations were given in JS94 and will not be repeated here. Following the same procedure, the equations for each azimuth radiance component (here we omit the index denoting the order of Fourier series) can be derived, which are in the atmosphere,

$$\mu_i^a \frac{\mathrm{d}I(\tau,\ \mu_i^a)}{d\tau} = I(\tau,\ \mu_i^a) - \sum_{\substack{j=-N_1 \\ j\neq 0}}^{N_1} \omega_j^a D(\tau,\ \mu_i^a,\ \mu_j^a) \times I(\tau,\ \mu_j^a) + X_0(\tau,\ \mu_i^a)\exp(-\tau/\mu_0), \quad i = \pm 1,\ \pm 2, \ldots,\ \pm N_1; \quad \tau \le \tau_a \tag{3a}$$

and in the ocean,

$$\mu_i^o \frac{\mathrm{d}I(\tau,\ \mu_i^o)}{d\tau} = I(\tau,\ \mu_i^o) - \sum_{\substack{j=-N_2 \\ j\neq 0}}^{N_2} \omega_j^o D(\tau,\ \mu_i^o,\ \mu_j^o) \times I(\tau,\ \mu_j^o),\ i = \pm 1,\ \pm 2, \ldots,\ \pm N_2; \quad \tau > \tau_a. \tag{3b}$$

Equations (3a) and (3b) are analogous to Eqs. (7) and (8) in JS94, but with different source terms. Here $2N_1$ and $2N_2$ are the numbers of quadrature points (i.e., stream numbers) applied in the atmosphere and ocean, respectively. $D(\tau, \mu_i, \mu_j)$ and $X_0(\tau, \mu_i)$ were also defined in JS94. The (μ_i^a, ω_i^a) and (μ_i^o, ω_i^o) are quadrature points and weights for the atmosphere and ocean, respectively, with $\mu_{-i} = -\mu_i$ and $\omega_{-i} = \omega_i$. They have the following relationships:

$$\mu_i^o = \sqrt{1 - [1 - (\mu_i^a)^2]/(n_w/n_a)^2}, \qquad i = 1,\ 2, \ldots,\ N_1, \tag{4}$$

$$\omega_i^o = \frac{n_a^2 \mu_i^a}{n_w^2 \mu_i^o}\,\omega_i^a, \qquad i = 1,\ 2, \ldots,\ N_1. \tag{5}$$

Here n_a and n_w represent the refractive indices of air and water, respectively. Following the same procedure as in JS94, the solutions for Eqs. (3a) and (3b) can be obtained as

$$I(\tau,\ \mu_i^a) = \sum_{j=1}^{N_1} \left[C_{-j} G_{-j}(\mu_i^a)\exp(k_j^a \tau) + C_j G_j(\mu_i^a) \times \exp(-k_j^a \tau)\right] + Z_0(\mu_i^a)\exp(-\tau/\mu_0), \quad i = \pm 1,\ \pm 2, \ldots,\ \pm N_1; \quad \tau \le \tau_a, \tag{6a}$$

$$I(\tau,\ \mu_i^o) = \sum_{j=1}^{N_2} \left[C_{-j} G_{-j}(\mu_i^o)\exp(k_j^o \tau) + C_j G_j(\mu_i^o) \times \exp(-k_j^o \tau)\right], \quad i = \pm 1,\ \pm 2, \ldots,\ \pm N_2; \quad \tau > \tau_a, \tag{6b}$$

where C_j and C_{-j} are constants of integration to be determined by the application of boundary and continuity conditions as discussed below. k_j and G_j are eigenvalues and eigenvectors, respectively, determined by solving an algebraic eigenvalue problem as described by Stamnes *et al.*[11] $Z_0(\mu_i^a)$ is defined and obtained by solving Eq. (12b) in JS94. The solutions represented by Eqs. (6a) and (6b) are seemingly simpler than those in JS94 for the flat ocean case. However, the solution is not complete yet, because constants $C_{\pm j}$ in Eqs. (6a) and (6b) are still unknowns, which differ from layer to layer in the atmosphere and the ocean (for simplicity, we omitted the index denoting layers here). These constants will be determined by boundary and interface conditions for radiances (intensities). The conditions for the top and bottom boundaries, for the interfaces among atmospheric layers, and for the interfaces among oceanic layers are the same as those for the flat ocean case, which were given by Eqs. (16a), (16b), (16f), and (16g) in JS94. However, the continuity conditions for radiances at the interface between the atmosphere and the ocean are very different from those for the flat ocean case. If we denote τ_a^- as the optical depth just above the ocean surface (i.e., the mean sea level) and τ_a^+ as that just below the surface, these conditions for the rough surface case can be expressed as

$$I(\tau_a^-,\ \mu_i^a) = \sum_{j=1}^{N_1} I(\tau_a^-,\ -\mu_j^a) R(\mu_i^a,\ \mu_j^a,\ n_w/n_a) + \sum_{j=1}^{N_2} I(\tau_a^+,\ \mu_j^o) T(\mu_i^a,\ \mu_j^o,\ n_a/n_w) + \frac{1}{\pi}\mu_0 F_0 \exp(-\tau_a/\mu_0) R(\mu_i^a,\ \mu_0,\ n_w/n_a), \quad i = 1,\ 2, \ldots,\ N_1, \tag{7}$$

$$I(\tau_a^+,\ -\mu_i^o) = \sum_{j=1}^{N_1} I(\tau_a^-,\ -\mu_j^a) T(\mu_i^o,\ \mu_j^a,\ n_w/n_a) + \sum_{j=1}^{N_2} I(\tau_a^+,\ \mu_j^o) R(\mu_i^o,\ \mu_j^o,\ n_a/n_w) + \frac{1}{\pi}\mu_0 F_0 \exp(-\tau_a/\mu_0) T(\mu_i^o,\ \mu_0,\ n_w/n_a), \quad i = 1,\ 2, \ldots,\ N_2, \tag{8}$$

in which reflection R and transmission T matrices appear without indices denoting the Fourier order. Equations (7) and (8) show that the emerging radiance at any direction at the air–water interface depends on incidences from all directions from both the atmosphere and the ocean for the rough ocean case. This contrasts with the simple one-to-one correspondence (pairing of each μ_i^a and μ_i^o) as presented by Eqs. (16c)–16(e) in JS94 for the radiances across the air–water interface of a flat ocean. One asset of the rough ocean case is the term accounting for the diffusion of the solar beam [the last term in Eqs. (7) and (8)]; it makes a simpler formulation of the particular solution [Eqs. (6a) and (6b)] than for the flat ocean case in JS94. The reflection and transmission matrices are calculated as

$$R(\mu,\ \mu',\ n) = \frac{2-\delta_{m0}}{2\pi}\int_0^{2\pi} \tilde{R}(\mu,\ \phi,\ \mu',\ \phi',\ n) \times \cos m(\phi-\phi')d(\phi-\phi'), \quad (9)$$

$$T(\mu,\ \mu',\ n) = \frac{2-\delta_{m0}}{2\pi}\int_0^{2\pi} \tilde{T}(\mu,\ \phi,\ \mu',\ \phi',\ n) \times \cos m(\phi-\phi')d(\phi-\phi'), \quad \delta_{m0} = \begin{cases} 1, & \text{if } m = 0, \\ 0, & \text{otherwise.} \end{cases} \quad (10)$$

Here $\tilde{R}(\mu, \phi, \mu', \phi', n)$ and $\tilde{T}(\mu, \phi, \mu', \phi', n)$ represent the reflection and transmission functions at the rough surface, respectively (see Appendix A). (μ', ϕ') and (μ, ϕ) are the incident and exit light directions, respectively. Note that, in these functions, n is the relative refractive index, which equals n_w/n_a if the incident light is from the air (n_a/n_w if the incidence is from the ocean). The reflectance and transmittance at the rough surface is closely related to the slope distribution of the surface facets. This distribution is usually expressed as a Gaussian function as[1]

$$P(\mu_n) = \frac{1}{\pi\sigma^2}\exp\left(-\frac{1-\mu_n^2}{\sigma^2\mu_n^2}\right), \quad (11)$$

where μ_n is the cosine of the normal to the surface facet. The σ is the mean slope distribution width and, based on Cox and Munk,[1] it is related to the windspeed U (m/s) as

$$\sigma^2 = 0.003 + 0.00512U. \quad (12)$$

The shadowing effect and multiple scattering (reflection) among the surface wave facets are also taken into account in the reflection and transmission functions.[12,13] More details about functions [$\tilde{R}(\mu, \phi, \mu', \phi', n)$ and $\tilde{T}(\mu, \phi, \mu', \phi', n)$] are provided in Appendix A. Substituting Eqs. (6a) and (6b) into the boundary and interface conditions [i.e., Eqs. (16a), (16b), (16f), and (16g) in JS94 and Eqs. (7) and (8) here], we obtain a system of linear algebraic equations for the unknown coefficients C_j. The method to solve the equations and obtain the unknown coefficients was described by Stamnes *et al.*[11] and is not repeated here. The implementation of these solutions into the CDISORT code is not trivial, however.

3. Examples of Model Simulations

A. Brief Description of the Model

The CDISORT just described has been used as the radiative transfer solver by our coupled ocean–atmosphere radiative transfer (COART) model[14,15] (http://www-cave.larc.nasa.gov/cave/). CDISORT accounts for the change in refractive index at the air–sea interface[9] and now includes the interface roughness into the analytic solution of the radiative transfer equation. Hence COART considers the atmosphere and ocean as one system and treats the ocean strata just as additional atmospheric layers with different optical properties. Similar to the atmosphere, the ocean can also be divided into an arbitrary number of layers required to resolve the vertical variations of the water properties. COART models the absorption and scattering processes in the atmosphere and ocean explicitly. These include the scattering and absorption by molecules, aerosols, and clouds in the atmosphere, and by liquid water molecules, dissolved and particulate matter in the ocean.

COART calculates radiances and irradiances at any level of the atmosphere and ocean in both narrowband (spectral) and broadband. For the narrowband scheme, users can specify both the band (wavelength) limits and computational resolution arbitrarily. In this scheme, COART employs the LOWTRAN 7 band model (spectral resolution of 20 cm^{-1}) and the molecular absorption database for the atmosphere. This corresponds to a wavelength resolution of approximately 0.5 nm at 500 nm and 8 nm at 2000 nm. For efficient broadband calculations of radiance and irradiance, COART divides the solar spectrum (0.20–4.0 μm) into 26 fixed wavelength intervals; in each spectral interval, the k-distribution technique parameterizes molecular absorption in the atmosphere using the HITRAN 2000 database.[16]

The most prominent effects of ocean surface roughness on solar radiation are on upwelling fields in the atmosphere and downwelling fields in the ocean. Its effects on the downwelling radiation in the atmosphere and the upwelling radiation in the ocean are significantly smaller. While COART can simulate a variety of quantities, including the water-leaving radiance, we show here mainly the types of calculations that pertain to surface roughness.

B. Effects of Surface Roughness on Radiance

The COART calculations in Fig. 1, which use a McClatchey mid-latitude summer atmosphere[17] with a marine aerosol optical depth of 0.1 (at 500 nm) and case 1 water for the ocean[18] with a chlorophyll concentration of 0.1 mg/m^3, span the upwelling radiance distribution at the top of the atmosphere (TOA) and the downwelling radiance distribution at four depths in the ocean (0, 10, 100, and 200 m) for three different wind speeds. The average Petzold[19] phase function for marine particle scattering is used in the calculations. Figure 1 uses polar coordinates, with view zenith angle (θ) on the radial axis and relative azimuth angle (ϕ) as the azimuthal coordinate. To facilitate comparisons of different wind speeds, wavelengths, and levels, the radiance in Fig. 1 is normalized by the upwelling or downwelling irradiance (E) at the same level to obtain the anisotropic radiance function (ARF) as

$$\mathrm{ARF}(\theta,\ \phi) = \frac{\pi I(\theta,\ \phi)}{E}, \quad (13)$$

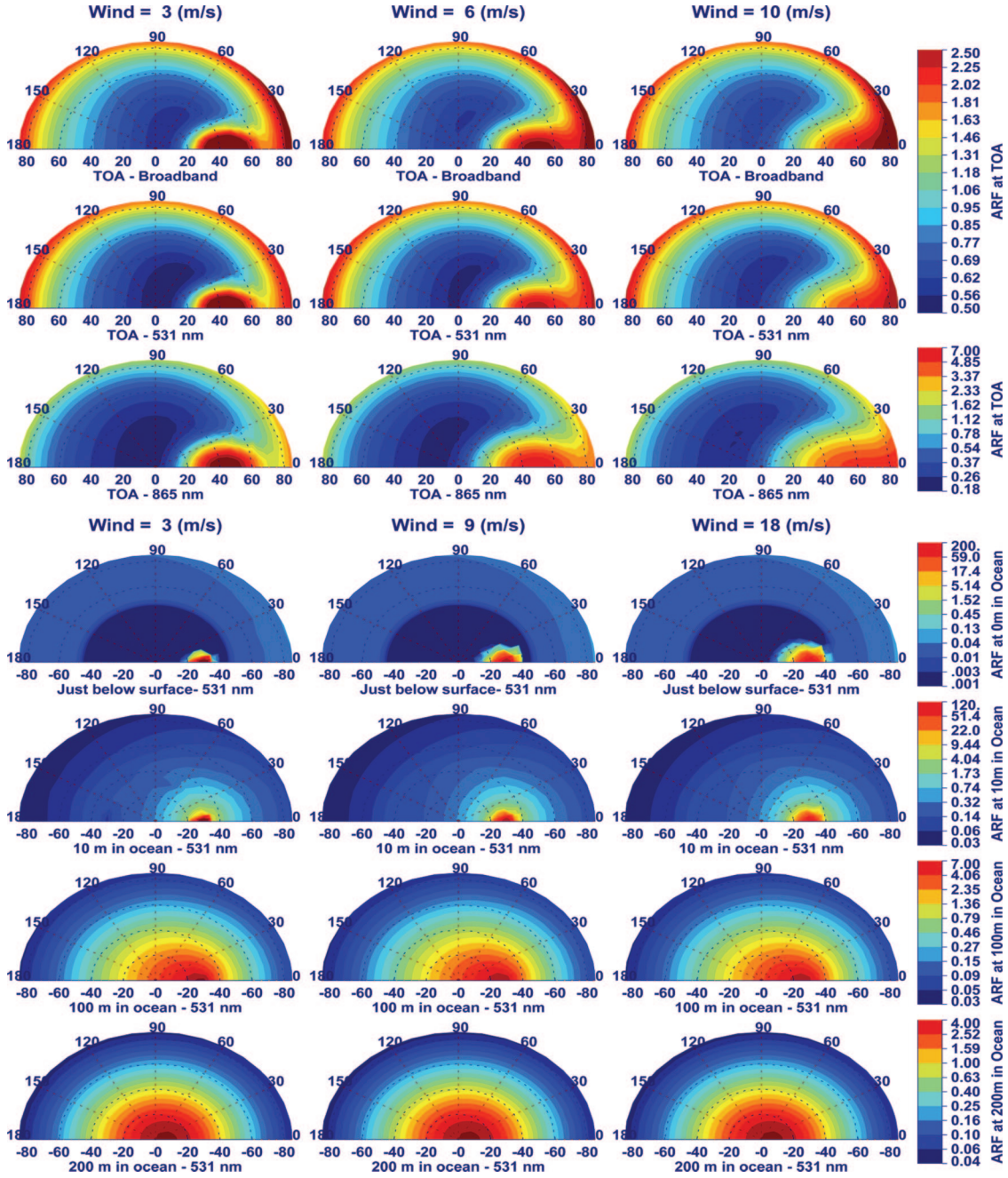

Fig. 1. Model-simulated upwelling radiance field at the TOA and the downwelling radiance field at depths of 0, 10, 100, and 200 m in the ocean for three different wind speeds and for three wavelength sets (broadband, narrowband at 531 nm, and narrowband at 865 nm). The SZA is 40°.

where E is the upwelling irradiance if $I(\theta, \phi)$ is the upwelling radiance (θ is positive in this case in Fig. 1) and otherwise, E is the downwelling irradiance (θ is negative in this case). The ARF here is, in fact, the ratio of the actual radiance, $I(\theta, \phi)$, and the imagined isotropic radiance, E/π, with the same irradiance. Therefore the gradient in the ARF represents the departure of the radiance field from the isotropic case (ARF = 1.0).

The solar zenith angle (SZA) in Fig. 1 is 40°. Because the slope distribution in Eq. (11) is independent of the wind direction, the ARF (and the radiance field itself) of Fig. 1 is symmetric with the principal plane (the vertical plane containing the Sun, the surface target, and the nadir). So only the ARF for the azimuth from 0° to 180° is presented. The entire principal plane is covered by the horizontal axis of each panel in Fig. 1, and the Sun (observer) is on the left (right). The top three rows of Fig. 1 show upwelling ARF for the broadband shortwave (0.20–4.0 μm), 531 nm [the central wavelength of the Moderate Resolution Imaging Spectroradiometer (MODIS) channel 11], and 865 nm (MODIS channel 16), respectively. The bottom four rows show the downwelling ARF at

four ocean depths for 531 nm only (865 nm is not shown because of strong absorption by liquid water, and the broadband is not shown because it is similar to 531 nm).

The three columns of Fig. 1 cover wind speeds of 3, 6, and 10 m/s for the atmospheric ARF and wind speeds of 3, 9, and 18 m/s for the ocean ARF. The hot spot in each panel represents the specular reflection (the sunglint in the atmosphere) or transmission (in the ocean) of the solar beam at the rough surface. The sunglint is conspicuous at the right of each TOA panel (top three rows), but the sunglint region widens as wind speed increases and is much more prominent for the 865 nm case because of less atmospheric scattering. Because the downwelling radiation in the upper ocean is sharply focused around the refracted solar beam, a larger wind variation than for the atmosphere is required to show the hot spot variation with wind (i.e., the widening as wind increases). As the depth in the ocean increases, however, the sharp radiance peak around the refracted solar beam rapidly decreases, and the position of the maximum radiance gradually shifts from the refracted solar zenith direction to the nadir. At deep ocean levels, the diffusion by ocean water and particles becomes more important, and the wind effect on the ARF or the radiance anisotropy diminishes. Eventually, the radiance distribution in deep water will approach an asymptotic shape with a maximum at the nadir, and the directional and depth dependences of the radiance distribution decouple. The asymptotic distribution is independent of the surface roughness or wind speed but dependent only on the inherent optical properties (IOPs) of the ocean. However, the speed with which this approaches an asymptotic distribution depends on both the ocean IOPs and the surface roughness. The radiance distribution approaches the asymptotic shape faster for a high-scattering water than for a high-absorption water, and faster for a high wind than for a low wind.

For the same atmospheric and ocean inputs, Fig. 2 further shows the radiance distribution at 531 nm only; and just around the hot spots in Fig. 1 in the principal plane, where radiance varies most sharply and wind effect is most glaring. Figure 2 highlights the different impacts of wind on the radiance fields at various levels in the atmosphere and ocean. Three different wind speeds (3, 6, and 9 m/s) are used here. Note, the radiance in the sunglint region at the TOA could be larger than at the surface when wind is weak, because the reflected solar radiances at the surface in this particular small region are much larger than the radiances outside; and the Rayleigh and aerosol radiances at the TOA are not enough to compensate for the attenuation of the strong reflected solar radiance at the surface. While the color scale of row 5 in Fig. 1 revealed virtually no effect of surface roughness on downwelling radiance broadly over the hemisphere, rows 2 and 3 of Fig. 2 show that wind, indeed, has an impact on the radiance distribution around the forward-scattering direction in the ocean. Figure 2 further delineates how the wind effect diminishes, and the radiance anisotropy rapidly decreases, as the depth in the ocean increases.

Figure 3 shows a model-observation comparison of the shortwave radiances at the TOA. The measurement data were from NASA's Cloud and Earth Radiation Energy System (CERES) instrument[20] during a special field program at the CERES Ocean Validation Experiment (COVE) site.[21] The CERES concerns radiation energy budget over the global ocean. The COVE site may not be strictly the case 1 water. However, *in situ* measured ocean optical properties [absorptions for phytoplankton and nonpigment particles, and for colored dissolved organic matter (CDOM)] instead of the parameterization for case 1 water were directly used in the model. The CERES was programmed to a special mode for intense observation at the COVE, and only the measurements in those clear days during the field experiment are presented here. In this experiment, comprehensive measurements on a variety of physical and optical properties of the atmosphere, surface, and ocean were also available for the model input here. The horizontal coordinate in Fig. 3 is the sunglint angle, defined as the angle between the view direction and the specular solar reflecting direction for an imagined flat surface. The nine numbers in the lower portion of Fig. 3 are the mean model-observation biases for the nine glint-angle intervals (10° each) from 0° to 90°, respectively. Though the aerosol loadings and the surface and ocean properties were different for different days, the model and observation agree fairly well away from the sunglint region. The difference is somewhat larger near the sunglint center (smaller glint angles), probably due to the error in the surface roughness treatment in the calculations, for example, the uncertainties in the Cox–Munk model. The SZA is approximately 20° when the CERES took the measurements, and so a large glint angle (larger than 75 in Fig. 3) also represents a large-view zenith angle, where the view path is longer and the surface footprint is larger, and therefore, the possible horizontal variations of the aerosol and the surface have larger effects than at a small-view angle. This might be responsible for the increased biases in the large-angle regime.

C. Effects of Surface Roughness on Irradiance and Albedo

The effects of ocean surface roughness on irradiances are shown in Fig. 4, which has upwelling irradiances in the atmosphere (linear scale) and downwelling irradiances (logarithmic scale) in the ocean for 531 and 865 nm, and the broadband shortwave (the three columns) at four different levels (the four rows). The model inputs for the atmosphere and ocean are identical in Figs. 1 and 4. In each panel of Fig. 4, the irradiances for different wind speeds are presented as a function of the cosine of the SZA. Results for a flat ocean case (wind = 0 m/s) are plotted as solid curves in each panel, and thus the difference of irradiances between a rough ocean case (represented by a nonzero wind) and the flat ocean case represents the

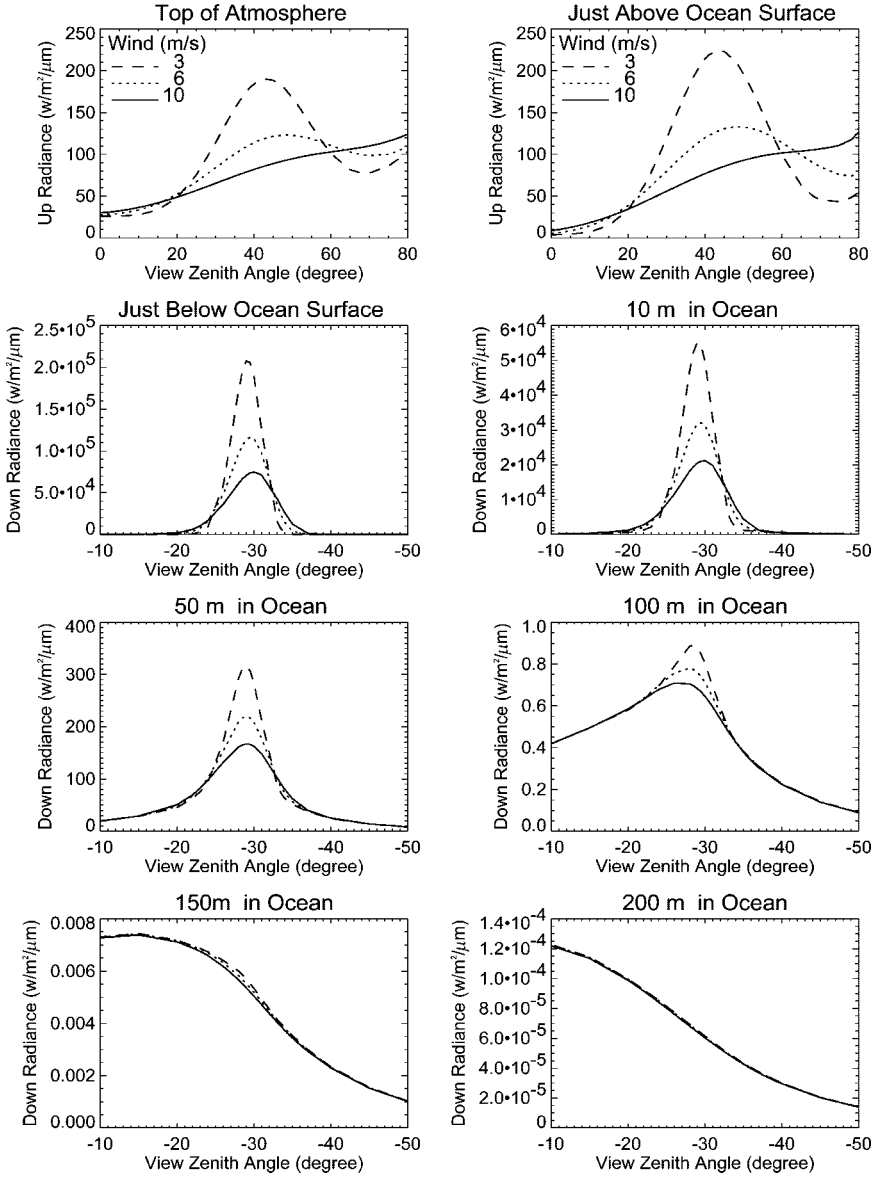

Fig. 2. Effects of surface roughness on radiance distributions at 531 nm in the components of the principal plane containing most of the reflected solar beam in the atmosphere (top row), and most of the refracted solar beam in the ocean (rows 2–4). The SZA is 40°.

surface roughness effect quantitatively. Figure 4 shows that the effect of surface roughness is smaller for high Sun than for low Sun; and the upwelling irradiance just above the surface (row 2) is the field with the most action. Note that for upwelling irradiance at low Sun, roughness has a larger effect at 865 nm (where much of the downwelling irradiance is direct, striking the surface at a glancing angle, thereby obtaining strong Fresnel reflection) than at 531 nm (where the downwelling irradiance is more diffuse and has a component that is closer to normal). However, we find the opposite for high Sun: roughness has a larger effect on above-surface upwelling irradiance at 531 nm than at 865 nm. The turning point is at approximately the SZA of 60 (cos SZA of 0.5), where the direct and diffuse reflectances are similar, and this angle can be considered as an effective angle for diffuse radiation. For each rough surface case, the variation with respect to the flat surface

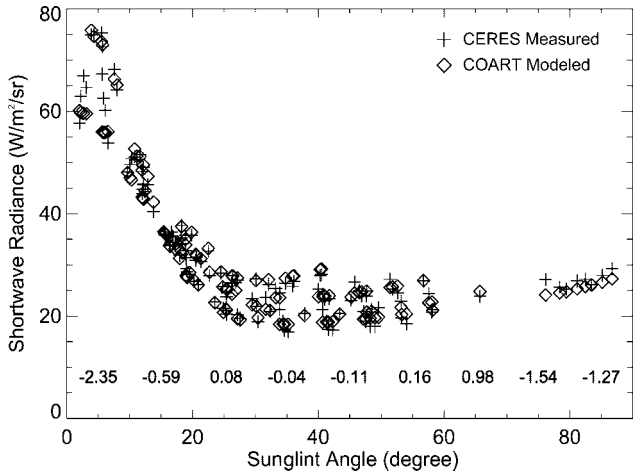

Fig. 3. Comparison of modeled and measured broadband radiances as a function of sunglint angle. The nine numbers are the mean model-observation biases for the nine glint-angle intervals (10° each) from 0° to 90°, respectively.

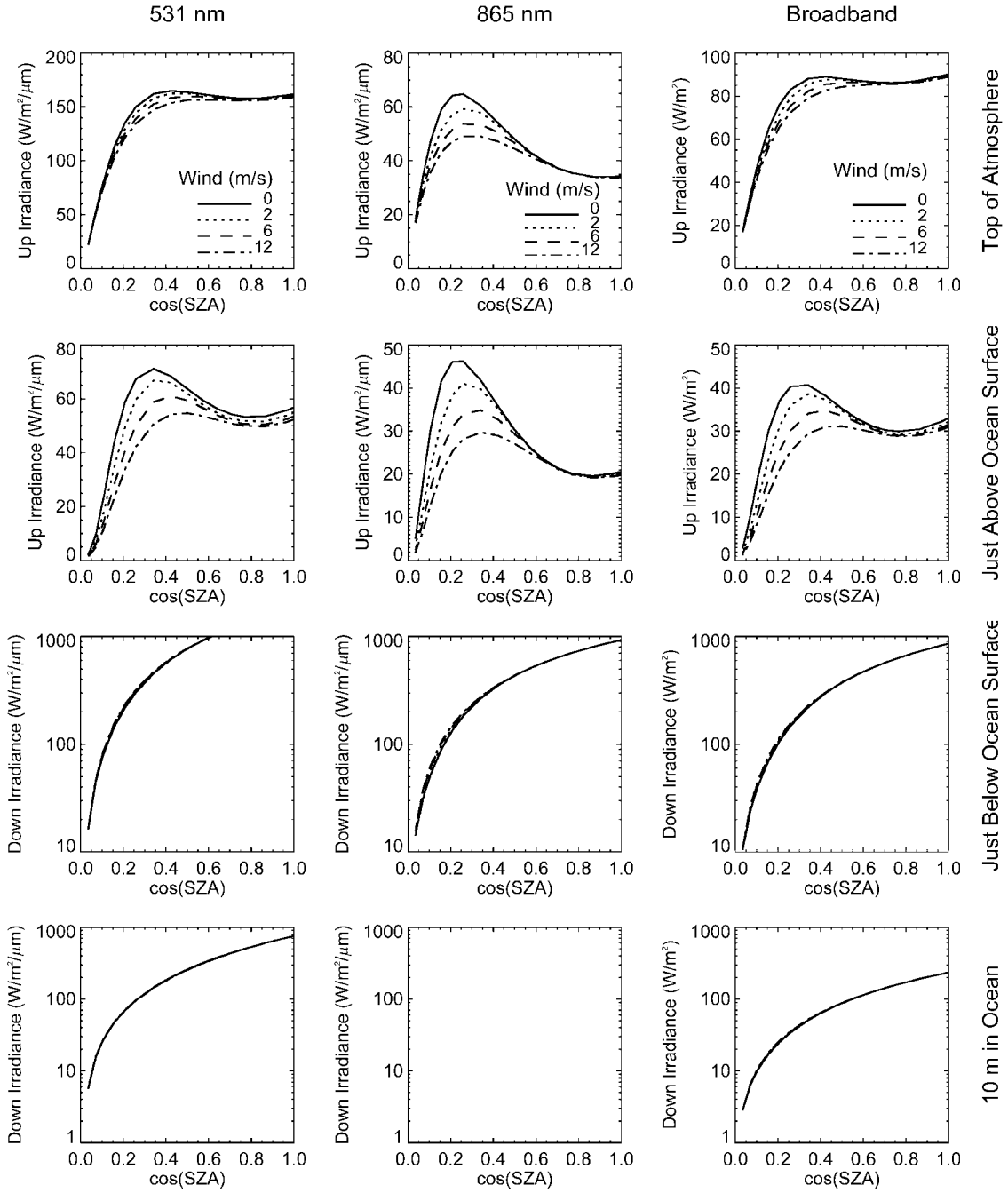

Fig. 4. Modeled irradiances versus cos(SZA) with upwelling irradiance in the atmosphere and downwelling irradiance in the ocean, for different wind speeds and different wavelengths.

case (the solid curve) in the downwelling irradiance just below the surface (row 3) is equivalent to the variation in the upwelling irradiance just above the surface (row 2) but with opposite sign. However, because the downwelling irradiance just below the surface is much larger than the upwelling irradiance just above the surface, the relative variation in the downwelling irradiance in the ocean from the flat ocean case to a rough surface case is smaller and is less obvious than in the upwelling in the atmosphere in Fig. 4, especially for high Sun conditions. At a depth of 10 m (row 4), the effects of internal ocean optics on irradiance outweigh the effects of surface roughness and the irradiance at 865 nm is none due to strong water absorption. At great depths, where the radiance distribution does not change, the irradiance attenuation also approaches a constant, dependent only on the ocean IOPs.

Because the downwelling irradiance in the atmosphere has little dependence on the surface condition of an ice-free ocean, the large effect of surface roughness on upwelling energy (top half of Fig. 4) will have a signal in the surface albedo. The left panel of Fig. 5 shows the multifilter rotating shawdowband radiom-

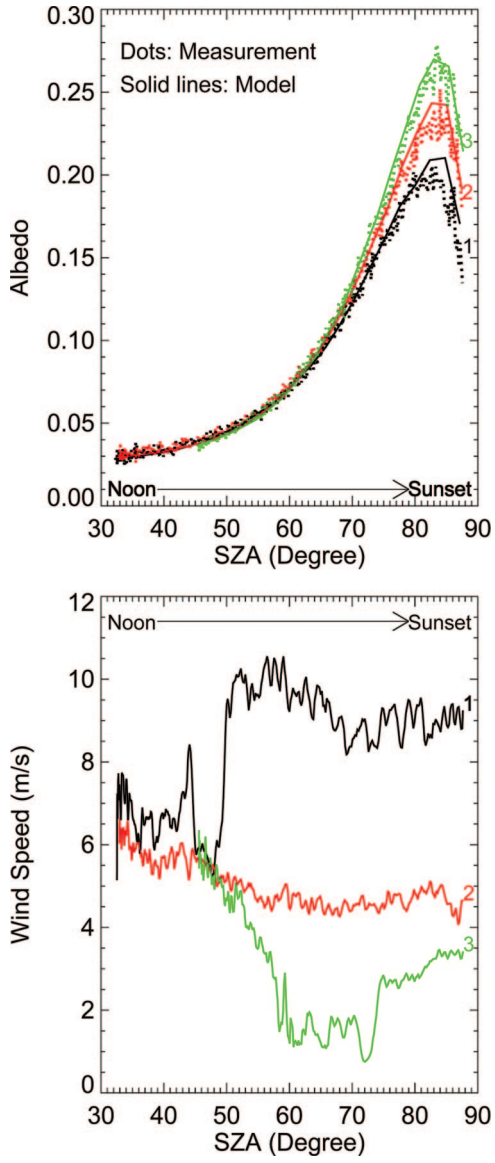

Fig. 5. Effects of wind speed on ocean surface albedo at 670 nm. The left panel shows the modeled and measured surface albedo during three afternoons. The right panel shows the observed wind speed for each afternoon. Different colors are for different days.

eter (MFRSR) measured (670 nm) (the dots) and modeled (the solid curves) surface albedo for three clear afternoons with quite different wind regimes (right panel) at the COVE; the aerosol loadings were low. Aerosol optical properties used in the model were measured from the same platform by NASA's Aeronet Cimel instrument.[22] The Cimel Sun photometer made periodic scans in the almucantar and in the solar principal plane; inversions of these data yielded aerosol phase functions and particle size distributions.[23] The wind data were from the National Oceanic and Atmospheric Administration meteorology station also at the COVE. The ocean optical properties and chlorophyll concentration were also from *in situ* measurements,[15] but ocean optics have little effect on the total surface albedo at 670 nm. To remove the relative difference between the two surface-based MFRSR instruments and obtain accurate ocean albedos, the instruments subsequently used for the downwelling and upwelling spectral irradiance measurements were calibrated relative to each other in advance, by observing the same target at the same time.[15,21] Results in Fig. 5 show the significant effects of wind on ocean surface albedo, especially for a large SZA. The dependences of albedos on the SZA and wind are consistent between model and measurements.

When light is incident on the rough surface at a grazing direction, the photons are more likely to undergo multiple scattering or reflection among the surface wave facets. There is also a shadowing effect of one wave facet blocking rays from getting to another facet (occultation).[13] Figure 6 shows the effects of multiple reflection and shadowing among the surface wave facets on albedo simulation. In each panel, the solid curve is the same modeled albedo as shown in Fig. 5, with both shadowing and multireflection considered. The short dashed curve is the calculation without shadowing but with multireflection, while the long dashed curve represents the results without any multireflection but with shadowing considered. The dotted curve is the calculation without roughness (flat surface). The error bar shows the range of mea-

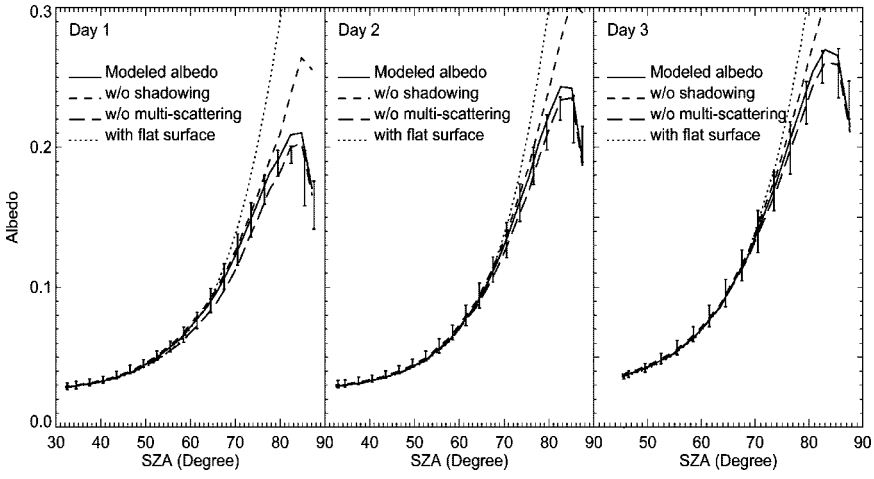

Fig. 6. Effects of multiple scattering (reflection) and shadowing among surface wave facets on ocean albedo simulation. The three panels are for the three selected days as in Fig. 5. The long dashed curve is the albedo computed without multireflection but with shadowing; the short dashed curve is the albedo computed without shadowing but with multireflection; the dotted curve is the albedo calculated with a flat surface. The error bar represents the measured albedo range to within 3° of the SZA.

sured albedo to within 3° of the SZA centered by the error bar. As expected, the calculated albedo is reduced after including the shadowing effect and is increased after including the multireflections. The effect of multireflection is larger on day 1 when the wind was high, and the model-observation agreement is improved after the effects of shadowing and multireflection are taken into account. However, the effects of shadowing and multireflection are small for high Sun (small SZA). The small differences between the flat ocean albedos (the dotted curves) are mainly due to the slightly different aerosol loadings for the three selected days.

Results above show that the surface roughness has the largest effect on ocean albedo at low Sun (large SZA). Both Figs. 5 and 6 show a larger model-observation discrepancy for a large SZA (higher than about 80) for the day with the strongest wind (day 1). This may indicate a larger error tendency in the Cox–Munk surface roughness model in high wind conditions. An alternate distribution was recently produced by Ebuchi and Kizu,[24] based on approximately 3×10^7 satellite observations over 5 years. The Ebuchi–Kizu function has a narrower slope distribution, and less sensitivity to wind, than the Cox–Munk function. The calculated albedo (not shown) based on the Ebuchi–Kizu model is close to that based on the Cox–Munk model for low winds, but higher for high winds and large SZAs. However, we cannot conclude the superiority of either the surface roughness parameterization, based on limited comparison. Validation of this parameterization is not a subject here. We simply indicate that the surface slope distribution function has a significant impact on the albedo calculation too. On the other hand, the radiative transfer model itself could also introduce errors for calculations with large SZAs. For example, we have not accounted for the orientation of the wave slope with the wind direction and the Earth curvature, both have larger impacts on glancing incidences.

4. Conclusion

We have presented an analytical approach for radiative transfer in a coupled atmosphere–ocean system having a rough surface between two media with differing indices of refraction. The discrete-ordinate technique is used in the formulation and solution. The solution is implemented in the radiative transfer code CDISORT. Using CDISORT as the radiative transfer solver, a coupled ocean–atmosphere radiative transfer model is now available to calculate various radiances and irradiances at any altitude in the atmosphere and depth in the ocean. This model is demonstrated online at http://www-cave.larc.nasa.gov/cave/ (search for "COART model" on Google).

Model simulations show that the ocean surface roughness has significant effects on the upwelling radiation in the atmosphere and the downwelling radiation in the ocean. As wind speed increases, the angular domain of sunglint broadens, the surface albedo under low Sun decreases, and transmission through the air–water interface to the interior of the ocean increases. The transmitted radiance just below the ocean surface is highly anisotropic, but this anisotropy decreases rapidly as the surface wind increases. Deeper below the surface, as the optical properties of the ocean interior eventually overcome the impact of surface roughness, the anisotropy decreases and the radiance distribution gradually approaches an asymptotic shape with a maximum at the nadir. The effects of surface roughness on radiation depend greatly on both wavelength and angle of incidence (i.e., solar elevation); these effects are significantly smaller throughout the spectrum at high Sun.

The models and observations agree fairly well on the effects of surface roughness. Some discrepancies may indicate that the original Cox–Munk surface roughness model is not sufficient for high wind conditions, or other errors exist in the treatment of the surface roughness.

Appendix A: Reflection and Transmission at a Rough Ocean Surface

The light incident at a flat water surface will be reflected or refracted directly. However, photons incident at the rough surface may scatter more than once among the surface wave facets before exit to air or water. The single-scattering reflectance at the air–water interface from (μ', ϕ') to (μ, ϕ) can be written as

$$R_0(\mu,\ \phi,\ \mu',\ \phi',\ n) = r(\cos\alpha_r,\ n) \times p(\mu',\ \phi' \to \mu,\ \phi,\ \mu_n^r,\ \sigma) \times s(\mu,\ \mu',\ \sigma), \quad \text{(A1)}$$

where $r(\cos\alpha_r, n)$ is the Fresnel reflection coefficient for relative refractive index n under incident angle α_r. $n = n_w/n_a$ for air incidence and $n = n_a/n_w$ for water incidence. The $p(\mu', \phi' \to \mu, \phi, \mu_n^r, \sigma)$ is the fraction of the sea surface (i.e., the effective area of the wave facets) with normal μ_n^r to reflect light from (μ', ϕ') to (μ, ϕ) and is given by

$$p(\mu',\ \phi' \to \mu,\ \phi,\ \mu_n^r,\ \sigma) = \frac{1}{4\mu(\mu_n^r)^4} P(\mu_n^r), \quad \text{(A2)}$$

where $P(\mu_n^r)$ is the surface slope distribution function given by Eq. (11). The required surface normal, μ_n^r, to fulfill the specular reflection from (μ', ϕ') to (μ, ϕ) is determined by μ', ϕ', μ, and ϕ. Defining

$$\cos\alpha = \mu\mu' + \sqrt{1-\mu^2}\sqrt{1-\mu'^2}\cos(\phi - \phi'), \quad \text{(A3)}$$

$\cos\alpha_r$ in Eq. (A1) can be derived as

$$\cos\alpha_r = \sqrt{(1+\cos\alpha)/2}, \quad \text{(A4)}$$

and μ_n^r can be derived as

$$\mu_n^r = \frac{\mu + \mu'}{\sqrt{2(1 - \cos\alpha)}}. \quad \text{(A5)}$$

In Eq. (A1), the shadowing effect, representing the probability that the incident and the reflected lights are intercepted by other surface waves, is corrected by the function $s(\mu, \mu', \sigma)$, which is based on Sancer[13] and is widely used.[5,7]

Similarly, the single-scattering transmittance at the air–water interface from (μ', ϕ') to (μ, ϕ) can be written as

$$T_0(\mu,\ \phi,\ \mu',\ \phi',\ n) = t(\cos\alpha_t,\ n) \times p(\mu',\ \phi' \to \mu,\ \phi,\ \mu_n^t,\ \sigma) \times s(\mu,\ \mu',\ \sigma), \quad \text{(A6)}$$

where $t(\cos\alpha_t, n)$ is the Fresnel transmission for relative refractive index n for incident angle α_t. $p(\mu', \phi' \to \mu, \phi, \mu_n^t, \sigma)$ is the fraction of the sea surface with the required orientation to refract light from (μ', ϕ') to (μ, ϕ) and is given by

$$p(\mu',\ \phi' \to \mu,\ \phi,\ \mu_n^t,\ \sigma) = \frac{n\sqrt{n^2 + \cos^2\alpha_t - 1}}{4\mu(\mu_n^t)^4 \cos\alpha_t} P(\mu_n^t). \quad \text{(A7)}$$

The surface normal (μ_n^t) and the incident angle (α_t) required to fulfill the refraction are

$$\cos\alpha_t = \frac{|n\cos\alpha - 1|}{\sqrt{n^2 - 2n\cos\alpha + 1}}, \quad \text{(A8)}$$

$$\mu_n^t = \mu'\cos\alpha_t + \sin\alpha_t\sqrt{1 - \mu'^2} \times \sqrt{1 - (1 - \mu^2)\sin^2(\phi - \phi')/\sin\alpha}. \quad \text{(A9)}$$

Due to the roughness nature, some photons after a first scattering at the surface may not exit to the air or water directly but experience a second or even higher orders of scattering processes. The reflectance and transmittance from these multiple scatterings can be derived from the single-scattering values (i.e., R_0 and T_0 represented by Eqs. (A1) and (A6) and the slope distribution function. For example, the second scattering reflectance from (μ', ϕ') to (μ, ϕ) is

$$R_1(\mu,\ \phi,\ \mu',\ \phi',\ n) = \int_{-1}^{1} \mathrm{d}\mu_1 \int_0^{2\pi} \mathrm{d}(\phi_1 - \phi') \times R_0(\mu_1,\ \phi_1,\ \mu',\ \phi',\ n) \times R_0(\mu,\ \phi,\ \mu_1,\ \phi_1,\ n), \quad \text{(A10)}$$

the third scattering reflectance is

$$R_2(\mu,\ \phi,\ \mu',\ \phi',\ n) = \int_{-1}^{1} \mathrm{d}\mu_2 \int_0^{2\pi} \mathrm{d}(\phi_2 - \phi') \times R_1(\mu_2,\ \phi_2,\ \mu',\ \phi',\ n) \times R_0(\mu,\ \phi,\ \mu_2,\ \phi_2,\ n), \quad \text{(A11)}$$

the fourth scattering reflectance is

$$R_3(\mu,\ \phi,\ \mu',\ \phi',\ n) = \int_{-1}^{1} \mathrm{d}\mu_3 \int_0^{2\pi} \mathrm{d}(\phi_3 - \phi') \times R_2(\mu_3,\ \phi_3,\ \mu',\ \phi',\ n) \times R_0(\mu,\ \phi,\ \mu_3,\ \phi_3,\ n), \quad \text{(A12)}$$

and so on for higher orders of scattering reflectance. Finally, the total reflectance is

$$\tilde{R}(\mu,\ \phi,\ \mu',\ \phi',\ n) = \sum_{i=0}^{N} R_i(\mu,\ \phi,\ \mu',\ \phi',\ n). \quad \text{(A13)}$$

This is the reflection function used in Eq. (9). Here $N + 1$ represents the highest order of multiple scattering to be considered. $N = 0$ is for single scattering only. In theory, N could be very large. But a large N means more computation time. In reality, most photons will be either reflected or refracted into the air or water after a single interaction with the surface. Photons could survive, for higher orders of successive multiple scattering decrease rapidly as the scattering order increases. Test results indicate that including the second scattering ($N = 1$) is sufficient for virtually all conditions.

Similar to the reflectance, the formulations for multiple-scattering transmittance can be written as

$$T_1(\mu,\ \phi,\ \mu',\ \phi',\ n) = \int_{-1}^{1} \mathrm{d}\mu_1 \int_0^{2\pi} d(\phi_1 - \phi') \times R_0(\mu_1,\ \phi_1,\ \mu',\ \phi',\ n) \times T_0(\mu,\ \phi,\ \mu_1,\ \phi_1,\ n), \quad \text{(A14)}$$

$$T_2(\mu,\ \phi,\ \mu',\ \phi',\ n) = \int_{-1}^{1} \mathrm{d}\mu_2 \int_0^{2\pi} d(\phi_2 - \phi') \times R_1(\mu_2,\ \phi_2,\ \mu',\ \phi',\ n) \times T_0(\mu,\ \phi,\ \mu_2,\ \phi_2,\ n), \quad \text{(A15)}$$

$$T_3(\mu,\ \phi,\ \mu',\ \phi',\ n) = \int_{-1}^{1} \mathrm{d}\mu_3 \int_0^{2\pi} d(\phi_3 - \phi') \times R_2(\mu_3,\ \phi_3,\ \mu',\ \phi',\ n) \times T_0(\mu,\ \phi,\ \mu_3,\ \phi_3,\ n), \quad \text{(A16)}$$

and then the total transmission used in Eq. (10) is

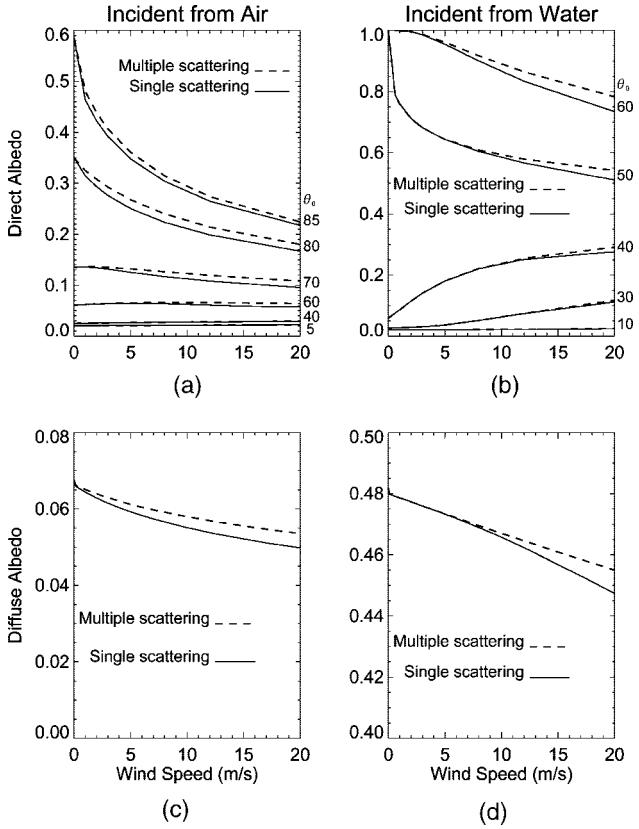

Fig. 7. Effect of multiple scattering between surface facets on the albedo. The upper two panels show the direct albedo (beam incidence) and the lower two panels show the diffuse albedo (isotropic incidence). The left panels are for incidence from air and the right panels are for incidence from water. The numbers by each pair of curves on the right of panels (a) and (b) represent the incident angles in degrees. For each pair of curves, the solid curve is for single scattering and the dashed curve is for multiple scattering.

$$\tilde{T}(\mu,\ \phi,\ \mu',\ \phi',\ n) = \sum_{i=0}^{N} T_i(\mu,\ \phi,\ \mu',\ \phi',\ n). \quad \text{(A17)}$$

The effects of multiple scattering on the total reflectance for a beam incidence (direct albedo) and for a diffuse incidence (diffuse albedo) are presented in Fig. 7. Albedo represents the irradiance reflectance. The direct albedo for a beam incidence from (μ_0, ϕ_0) is

$$RR(\mu_0) = \frac{1}{\mu_0}\int_0^{-1} \mathrm{d}\mu \int_0^{2\pi} d(\phi - \phi_0) \times \mu\tilde{R}(\mu,\ \phi,\ \mu_0,\ \phi_0,\ n). \quad \text{(A18)}$$

From the direct albedo, the diffuse albedo can be obtained by integrating RR weighted by the incident radiances. For the uniform (isotropic) incidence, this diffuse albedo is simply

$$R_{df} = 2\int_0^1 \mu RR(\mu)\mathrm{d}\mu. \quad \text{(A19)}$$

In Fig. 7, the upper two panels are for the direct albedo and the lower two panels are for the diffuse albedo. The left panels are for light incident from air ($n = 1.34$), and the right panels are for light incident from water ($n = 1/1.34$). Here the water refractive index of 1.34 is used, which is a typical number for visible wavelengths. The solid curves in Fig. 7 are for single scattering and the dashed curves are for multiple scattering. In panels (a) and (b), the numbers by each pair of lines on the right edge represent the incident angles. These results show that the multiple-scattering effect is small for radiation with small incident angles and increases as wind speed increases. Note, for a flat surface, the direct albedo is 1.0 (i.e., total reflection) for water-incident light with an incident angle larger than the critical angle (which is 48.2° for $n_w = 1.34$). Figure 7 (panel b) indicates that this total reflection region disappears when the surface is rough.

The total transmittance for a beam incidence or for a diffuse incidence simply equals one minus the total relevant albedo as defined in Eqs. (A18) and (A19). Therefore opposite to the albedo, the multiple scattering will decrease the transmittance across the air–water interface incident from either direction.

We thank the late Glenn Cota, Xiaojun Pan, David Rubble at Old Dominion University for the measurements of ocean optical properties, B. N. Holben of the NASA Goddard Space Flight Center for the Aeronet data, Fred Denn for the measurements at the COVE, and Fred Rose for help with the CERES data. This research was supported by NASA's Earth Observation System through the CERES. K. Stamnes is supported by NASA grant NRA-02-OES-06.

References

1. C. Cox and W. Munk, "Measurement of the roughness of the sea surface from photographs of the sun's glitter," J. Opt. Soc. Am. **44,** 838–850 (1954).
2. A. Morel and B. Gentili, "Diffuse reflectance of oceanic waters. II: bidirectional aspects," Appl. Opt. **32,** 6864–6879 (1993).
3. G. N. Plass and G. W. Kattawar, "Radiative transfer in the earth's atmosphere and ocean: influence of ocean waves," Appl. Opt. **14,** 1924–1936 (1975).
4. J. T. O. Kirk, "The upwelling light stream in natural waters," Limnol. Oceanogr. **34,** 1410–1425 (1989).
5. H. Gordon and M. Wang, "Surface-roughness considerations for atmospheric correction of ocean color sensors. I. The Rayleigh-scattering component," Appl. Opt. **31,** 4247–4260 (1992).
6. R. W. Preisendorfer and C. D. Mobley, "Albedos and glitter patterns of a wind-roughened sea surface," J. Phys. Oceanogr. **16,** 1293–1316 (1986).
7. T. Nakajima and M. Tanaka, "Effect of wind-generated waves on the transfer of solar radiation in the atmosphere-ocean system," J. Quant. Spectrosc. Radiat. Transfer **29,** 521–537 (1983).
8. J. L. Deuze, M. Herman, and R. Santer, "Fourier series expansion of the transfer equation in the atmosphere-ocean system," J. Quant. Spectrosc. Radiat. Transfer **41,** 483–494 (1989).
9. Z. Jin and K. Stamnes, "Radiative transfer in nonuniformly refracting layered media: atmosphere-ocean system," Appl. Opt. **33,** 431–442 (1994).
10. K. I. Gjerstad, J. Stamnes, B. Hamre, J. K. Lotsberg, B. Yan, and K. Stamnes, "Monte Carlo and discrete-ordinate simula-

tions of irradiances in the coupled atmosphere-ocean system," Appl. Opt. **42,** 2609–2622 (2003).
11. K. Stamnes, S. C. Tsay, W. Wiscombe, and K. Jayaweera, "Numerically stable algorithm for discrete-ordinate-method radiative transfer in multiple scattering and emitting layered media," Appl. Opt. **27,** 2502–2509 (1988).
12. L. Tsang, J. A. Kong, and R. T. Shin, *Theory of Remote Sensing* (Wiley, 1985).
13. M. I. Sancer, "Shadow-corrected electromagnetic scattering from a randomly-rough ocean surface," IEEE Trans. Antennas Propag. **AP-17,** 557–585 (1969).
14. Z. Jin, T. P. Charlock, and K. Rutledge, "Analysis of broadband solar radiation and albedo over the ocean surface at COVE," J. Atmos. Ocean. Technol. **19,** 1585–1601 (2002).
15. Z. Jin, T. P. Charlock, K. Rutledge, G. Cota, R. Kahn, J. Redemann T. Zhang, D. A. Rutan, and F. Rose, "Radiative transfer modeling for the CLAMS experiment," J. Atmos. Sci. **62,** 1052–1070 (2005).
16. S. Kato, T. P. Ackerman, J. H. Mather, and E. E. Clothiaux, "The *K*-distribution method and correlated-*k* approximation for a shortwave radiative transfer model," J. Quant. Spectrosc. Radiat. Transfer **62,** 109–121 (1999).
17. R. A. McClatchey, R. W. Fenn, J. E. A. Selby, F. E. Volz, and J. S. Garing, *Optical Properties of the Atmosphere,* AFCRL Rep. AFCRL-72-0497 (Air Force Cambridge Research Laboratories, Bedford, Mass. A, 1972).
18. A. Morel and S. Maritorena, "Bio-optical properties of oceanic waters: a reappraisal," J. Geophys. Res. **106**(C4), 7163–7180 (2001).
19. T. J. Petzold, *Volume Scattering Functions for Selected Ocean Waters* (Scripps Institution of Oceanography, 1977).
20. B. A. Wielicki, B. R. Barkstrom, E. F. Harrison, R. B. Lee, G. L. Smith, and J. E. Cooper, "Clouds and the Earth's radiant energy system (CERES): an Earth observing system experiment," Bull. Am. Meteorol. Soc. **77,** 853–868 (1996).
21. W. L. Smith, Jr., T. P. Charlock, R. Kahn, J. V. Martins, L. A. Remer, P. V. Hobbs, J. Redemann, and C. K. Rutledge, "EOS TERRA aerosol and radiative flux validation: an overview of the Chesapeake lighthouse and aircraft measurements for satellites (CLAMS) experiment," J. Atmos. Sci. **62,** 903–918 (2005).
22. B. N. Holben, T. F. Eck, I. Slutsker, D. Tanre, J. P. Buis, A. Setzer, E. Vermote, J. A. Reagan, Y. J. Kaufman, T. Nakajima, F. Lavenu, I. Jankowiak, and A. Smirnov, "AERONET—A federated instrument network and data archive for aerosol characterization," Remote Sens. Environ. **66,** 1–16 (1998).
23. O. Dubovik and M. D. King, "A flexible inversion algorithm for retrieval of aerosol optical properties from sun and sky radiance measurements," J. Geophys. Res. **105,** 20673–20696 (2000).
24. N. Ebuchi and S. Kizu, "Probability distribution of surface slope derived using sun glitter images from geostationary meteorological satellite and surface vector winds from scatterometers," J. Oceanogr. **58,** 477–486 (2002).